Regeneratively Cooled Multiple-Use Plug Hybrid for Nanosatellites

Shannon D. Eilers,* Stephen A. Whitmore,† and Zachary W. Peterson*
Utah State University, Logan, Utah 84322

DOI: 10.2514/1.B34778

The multiple-use plug hybrid for nanosatellites prototype thruster is being developed to fill a niche application for nanosat scale spacecraft propulsion. The prototype thruster uses safe-handling and inexpensive nitrous oxide and acrylonitrile-butadiene-styrene as propellants. The thruster system provides attitude control using secondary-injection thrust vectoring and allows large-impulse ΔV and small-impulse attitude control and proximity burns to be performed with the same system. To ensure survivability during extended duration burns, the multiple-use plug hybrid for nanosatellites incorporates a novel regenerative cooling design in which the nitrous oxide oxidizer flows through a cooling path embedded in the aerospike nozzle, before being injected into the combustion chamber near the nozzle base. Digital manufacturing was used to fabricate the nozzle components. Fused deposition modeling was used to fabricate the solid fuel grain from the acrylonitrile-butadiene-styrene thermoplastic. When fully developed, the multiple-use plug hybrid for nanosatellites thruster could provide an enhanced propulsive capability that would enable multiple nanosatellites to be independently repositioned after deployment from the parent launch vehicle. Because the environmentally benign propellants are mixed only within the combustion chamber after ignition, the system is inherently safe and can be piggybacked on a secondary payload with very little overall mission risk increase to the primary payload.

Nomenclature

A	=	area
B, b	=	empirical constant
C_d	=	discharge coefficient
$\bar{c}_p$	=	specific heat
D	=	diameter
F_s	=	side force generated by thrust vectoring
$f(Fr)$	=	fluid stratification parameter
G_{HEM}	=	mass flux from homogenous equilibrium model
G_{NHNE}	=	nonhomogeneous, nonequilbrium mass flux
$G_{s,f}$	=	material-specific constant
G_{SPI}	=	mass flux from incompressible model
g	=	acceleration of gravity
H_2	=	heat transfer coefficient
H_3	=	heat transfer coefficient corrected for curvature
h_1	=	fluid enthalpy before orifice
h_2	=	fluid enthalpy after orifice
I_{sp_s}	=	side-force specific impulse
k	=	nonequilibrium parameter
M	=	Mach number
$\dot{m}$	=	mass flow rate
$\dot{m}_s$	=	thrust-vectoring injectant mass flow rate
P	=	pressure
Pr	=	Prandtl number
q_w	=	heat flux into wall
q''	=	area-specific heat transfer rate
R_g	=	gas constant
r	=	local radius
St	=	Stanton number
s	=	curvilinear coordinate
T	=	temperature
U	=	fluid velocity
X	=	fluid quality
Re_Γ	=	Reynolds number based on boundary-layer thickness
β	=	empirical constant
Γ	=	boundary-layer thickness
γ	=	specific heat ratio
κ	=	thermal conductivity
μ	=	fluid viscosity
ρ	=	density
τ_b	=	bubble formation time constant
τ_r	=	fluid residence time constant
ω	=	empirical constant

Subscripts

h_{fg}	=	heat of vaporization
l	=	liquid parameter
v	=	vapor parameter
0	=	static fluid conditions
∞	=	local fluid conditions

Presented as Paper 2012-4199 at the 48th AIAA/ASME/SAE/ASEE Joint Propulsion Conference & Exhibit, Atlanta, Georgia, 30 July–1 August 2012; received 30 August 2012; revision received 15 May 2013; accepted for publication 16 May 2013; published online 2 August 2013.

*Graduate Research Assistant, Mechanical and Aerospace Engineering (MAE) Department, 4130 Old Main Hill. Student Member AIAA.

†Associate Professor, Mechanical and Aerospace Engineering (MAE) Department, 4130 Old Main Hill. Associate Fellow AIAA.

I. Introduction

THERE exists an emerging scientific, military, and commercial interest in constellations of small, inexpensive nanoscale spacecraft. Of particular interest are nanosatellites (nanosats), which can be flown as secondary payloads. A particular nanosat design that is seeing increasing popularity is a 10×10 cm cube form factor (1U). Multiple 1U cubes are coupled together to form "cubesats." Standard deployment systems for cubesats as large as 6U have currently been certified for flight on several U.S. and European launch vehicles.

If these small spacecraft can be deployed and organized into constellations to collectively perform a coordinated mission, they present distinct advantages not available to single larger-scale spacecraft that must be deployed one launch at a time. The distributed nature of this small spacecraft "swarm" offers a significant increase in mission reliability. A large constellation has built-in redundancy. Advanced space missions enabled by these orbiting constellations include 1) sun–Earth connection science missions that collect simultaneous multipoint spatial and temporal thermospheric and ionospheric data to analyze the causes and effects of space weather on the Earth, 2) persistent surveillance of Earth science targets, and 3) beyond-line-of-sight surface communications. Additional propulsive capability allows for advanced mission concepts. Providing a capability of approximately 800–1200 m/s (depending on orbital

inclination and specific mission requirements) allows a spacecraft to be deployed onto interplanetary trajectories from a standard geostationary transfer orbit. This capability could enable nanosat constellations to perform interplanetary missions.

Only a few specialized launch vehicles have upper stages with the ability for in-space restarts [1]; these are typically reserved for expensive government-owned reconnaissance, communications, or command and control satellites. For existing rideshare launch opportunities, nanoscale spacecraft are delivered to orbit as passive secondary payloads and must accept whatever orbit they achieve during the deployment process.

Secondary payloads, especially in the nanosat class, have no ability to modify their initial orbit and currently remain a novelty with little capability to accomplish serious scientific, strategic, or commercial missions. Thus, development of a propulsion unit that rides along with the secondary payload during launch, and then repositions or maintains the orbit after deployment, is highly desirable. Such a device would benefit the entire small satellite industry.

However, if this device were constructed using conventional volatile propellants, the "ride-along" payloads, each with their own propulsion system, would dramatically increase the risks to the primary payload. Managing this risk will result in prohibitive launch costs [2]. Thus, this "rideshare" propulsion unit must be developed using nontoxic propellants and must feature inherently safe designs. Hybrid-rocket motors have the potential to fulfill this low-risk flight requirement.

The multiple-use plug hybrid for nanosats (MUPHyN), which is the subject of this paper, was developed as a proof-of-concept for integrating several discrete features that allow the compactness of form factor required for nanosat propulsion. These features will be described in detail later in this paper. A primary design feature is the use of direct digital manufacturing methods to embed a helical structure into the fuel port. This helical structure allows for a significantly reduced combustion chamber length and dramatically increased fuel regression rates. Similarly, a second innovative design feature of the MUPHyN unit is an annular aerospike nozzle with secondary injection thrust vectoring. The aerospike configuration allows for a high expansion ratio in a length that is significantly shorter than a conventional minimum-length nozzle. Secondary injection allows for thrust vector deflection, essentially "gimbaling" of the nozzle exit plume with no mechanical apparatus other than injection ports and small injection valves. Successfully integrating these design features into a small form factor is a key step toward allowing a "universal" small satellite (smallsat) propulsion bus to be scaled and mass produced for a wide swath of smallsat missions. Although clearly detailed system capabilities and specifications are mission driven, Table 1 shows potential missions that can be achieved by a universal propulsion bus, derived from the MUPHyN design and scaled for 1 and 25 N thrust levels.

II. Inherent Safety of Hybrid-Rocket Systems

There are three types of chemically propelled rockets: liquid, solid, and hybrid. Bipropellant liquid engines mix and burn highly volatile oxidizer and fuel components in the combustion chamber. Solid-rocket motors use a propellant grain that binds both the oxidizer and fuel in a hydrocarbon substrate. Both liquid-rocket engines and solid-rocket motors have a potential for explosion. NASA estimated

Table 1 Potential mission matrix for scaled propulsion module

Spacecraft function	Spacecraft size	1 N	25 N
Drag offset	Any	X	— —
In-space maneuvering	Nano	X	— —
In-space maneuvering	Small/medium	X	X
Reaction wheel desaturation	Small/medium	X	— —
Station keeping	Any	X	X
Escape trajectory	Any	X	X
Formation flying	Any	X	X

Table 2 MUPHyN motor design parameters

Parameter	Value
Design thrust	200 N
Chamber pressure	690 kPa
Expansion ratio	2.25
Throat area	2.01 cm^2
Oxidizer	Nitrous oxide
Fuel	Acrylonitrile butadiene styrene
Design specific impulse	200 s
Design thrust vectoring side force	10 N
Secondary fluid	Helium, nitrogen, or oxygen

that the space shuttle's liquid-fueled main engines would fail catastrophically once every 1530 sorties [3,4] and the space shuttle solid-rocket boosters will fail catastrophically once every 1550 sorties. Even small solid-propelled ordnance motors intended for noncrewed spacecraft fail approximately one in every 250 burns [5]. The very significant explosion risk of liquid bipropellant or solid composite propellants has traditionally banned spacecraft with propulsion systems from flying as secondary payloads. A lower risk propellant option is highly desirable.

Traditional monopropellant liquid engines are also not without their share of hazards. Hydrazine is by far the most commonly used monopropellant for primary spacecraft propulsion and attitude control thrusters [6,7]. Hydrazine thrusters are relatively simple and consist of an electric solenoid valve, a pressurant tank, and a catalyst bed of alumina pellets impregnated with iridium or another transition metal. Unfortunately, hydrazine is a powerful reducing agent that poses serious environmental and health concerns. Hydrazine is extremely destructive to living tissues and is a known carcinogen. Exposure produces a variety of adverse systemic effects, including damage to liver, kidneys, nervous system, and red blood cells [8].

In contrast to traditional solid or liquid motors, hybrid-rocket motors separate the liquid oxidizer from the solid fuel grain and present little to no risk of explosion while burning. Because the fuel and oxidizer components of hybrid motors are often inert by themselves,[‡] the United States Department of Transportation classifies hybrid designs as presenting near zero potential for explosion during storage and handling [9]. Once deployed and separated from the main launch vehicle stage, the secondary payload presents minimal hazard to the primary payload and other secondary payloads. Other advantages of hybrid rockets include the capability for in-flight restart, throttling, easy ground handling, and relative insusceptibility to grain flaws. Optimized hybrid systems can offer vacuum specific impulses in excess of 300 s [10], yielding significantly greater performance than cold-gas or monopropellant systems (hydrazine thrusters typically have specific impulses in the range of 250 s [7]). Unfortunately, mostly due to typically low fuel surface regression rates, to achieve oxidizer-to-fuel (O/F) mass flow ratios that insure proper combustion characteristics, traditional hybrid motors have significantly long aspect ratios, where the motor length is often 10 times the major cross-sectional diameter. These long form factors are poorly suited for small-spacecraft applications. Thus, if hybrid motor designs are to be adapted for cubesat applications, unique design features must be incorporated to overcome this limitation.

III. Multiple-Use Plug Hybrid for Nanosats Thruster: Design Overview

The MUPHyN prototype is being developed to fill this niche application for nanosat and cubesat scale spacecraft propulsion systems. When fully developed, this propulsive unit could be integrated onto a cubesat payload and flown on rideshare missions with little risk increase to the primary payload.[§]

[‡]If improperly handled or mixed with fuel sources, nitrous oxide can exothermically decompose. However, these events are rare, even though use of nitrous oxide is extensive.

[§]It should be noted that waivers are required for any pressure vessel on a cubesat.

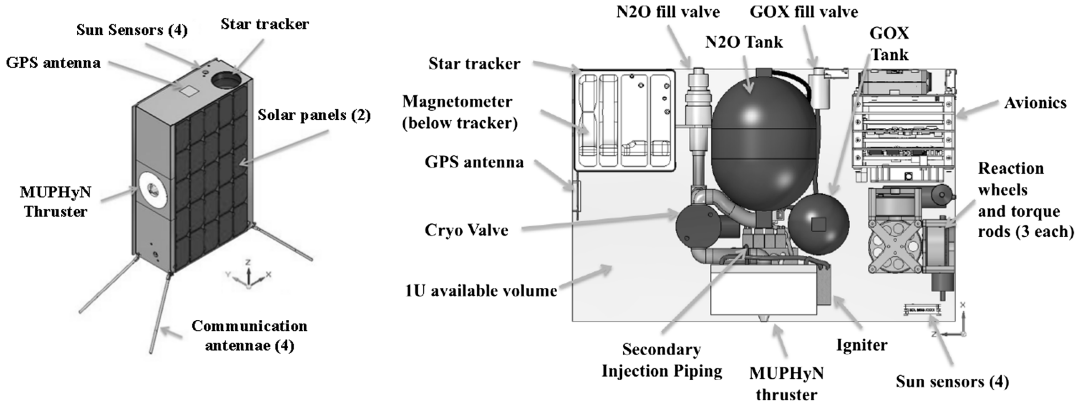

a) External View of Spacecraft b) Internal Layout of Spacecraft Components

Fig. 1 Proposed 6U cubesat MUPHyN thruster propulsion system.

Volumetric efficiency is a prime consideration for cubesat systems, thus compactness and simplicity are key system design elements for the MUPHyN systems. Because of this volumetric limit, conventional propulsion systems with high expansion ratio gimbaled nozzles and reaction control thrusters are infeasible in the cubesat form factor. The cubesat scale is simply too small to allow the complex mechanical subsystems to be integrated while still leaving room for the payload and supporting avionics.

Table 2 lists the design parameters for the proof-of-concept MUPHyN thruster as tested during this development campaign. Although this non-flight weight configuration is rather large for nanosat applications, the scale of this prototype unit is one that could be cost-effectively manufactured using the machining capabilities readily available to the research team at Utah State University. The MUPHyN thruster offers several features that are uniquely suited for nanosat and, particularly, cubesat applications. These features include 1) a highly compact truncated aerospike nozzle, 2) nonmechanical thrust vectoring using secondary fluid injection on the aerospike nozzle, 3) a hybrid fuel grain with an embedded helical port, and 4) a nonpyrotechnic ignition system. This synthesis of technologies is unique to the MUPHyN thruster design and no other commercial or government entity has produced comparable work that has been published in open literature. The resulting system is compact, nontoxic,¶ nonexplosive, and uses nonpyrotechnic means for reliable motor ignition. The system offers the simplicity of a monopropellant thruster but provides significantly higher specific impulse performance.

The MUPHyN thruster design featuring a helical fuel grain and aerospike nozzle offers a very volumetrically efficient combustion chamber configuration. The MUPHyN-equivalent MR-107B 180N hydrazine monopropellant thruster developed by Aerojet has a total length of 18.7 cm, significantly longer than the MUPHyN chamber [11].

Figure 1 presents a 6U cubesat design proposed for the NASA Edison flight demonstration program [12], which features the MUPHyN thruster as its primary propulsion system. Figure 1a shows the external view of the spacecraft. Figure 1b shows the internal layout of the MUPHyN subsystem components, including the liquid-propellant tanks and the gaseous oxygen (GOX) tanks used to supply a top pressure to the propellant delivery systems. In this configuration, GOX would serve as an ignition source as well as a pressurant. Supporting avionics and auxiliary attitude control subsystems are also shown.

A. Leveraging the Aerospike Nozzle for the MUPHyN Design

Although the aerospike nozzle has well-known altitude compensation capability during endoatmospheric flight, it also presents significant advantages for exoatmospheric applications. Because of its unique shape, the aerospike nozzle can be constructed with a higher area expansion ratio and more compact form factor than a conventional bell nozzle of the same mass. The higher expansion ratio provides better performance in a space environment; the compact form factor offers significant improvement in volumetric efficiency. Most important, the aerospike nozzle can be thrust vectored fluid dynamically by injecting propellant asymmetrically near the nozzle base.

The MUPHyN configuration exploits these advantages to develop a very compact system that employs secondary injection on a truncated annular aerospike nozzle for thrust-vectoring. A secondary fluid is injected near the end of the aerospike nozzle to deflect the plume, and fluid-mechanical interactions with the primary flowfield creates a high-pressure region upstream of the secondary injection port. This interaction amplifies the side force created by the secondary injection. Cold gas tests have shown that this amplification factor, defined as the ratio of the side-force specific impulse with main flow active to side-force specific impulse without main flow active, approaches 140% [13].

Additionally, because the orifices used for secondary injection are external to the spacecraft and are not constrained by an external nozzle boundary, these ports can be used for reaction control without the primary thruster operational. When this vectoring potential is harnessed and incorporated into a controlled thrust-vectoring scheme, there exists a significant potential for two-axis attitude control with a single MUPHyN thruster, or three-axis control with two MUPHyN thrusters without mechanical nozzle gimbals.

B. Applications of Digital Manufacturing

Advancements in digital manufacturing (often referred to as rapid prototyping) have revolutionized a variety of industries in recent years and offer a similar potential for hybrid-rocket motor design and manufacture. In particular, complex or difficult to cast grain geometries, especially on a small scale, are well suited to rapid prototyping techniques.

A major result of research just recently completed by Whitmore et al. at Utah State University (USU) [14] was the demonstrated viability of thermoplastic as a hybrid-rocket fuel grain material. This research demonstrated that, when coupled with nitrous oxide (N2O) as the oxidizer, acrylonitrile-butadiene-styrene (ABS) burns with a specific impulse I_{sp} that is approximately 6% lower than the traditional hybrid-rocket fuel hydroxyl-terminated polybutadiene (HTPB) without any formulaic changes to the ABS. ABS and HTPB fuel regression rates were measured to be nearly identical. It is anticipated that ABS could be optimized for fuel performance to yield even higher specific impulses.

Unlike HTPB, which is a thermosetting material, ABS is a thermoplastic that melts before vaporizing when subjected to heat. This property makes ABS one of the materials of choice for fused deposition modeling (FDM) rapid prototyping machines. Because ABS can be formed into a wide variety of shapes using modern additive manufacturing and rapid prototyping techniques, it is possible to embed complex high surface area flowpaths within the

¶At very high concentrations, nitrous oxide is an asphyxiant, but at moderate concentrations, it is usually considered nontoxic or minimally toxic. Nitrous oxide is a very common anesthetic and analgesic, and so its health effects are relatively well known.

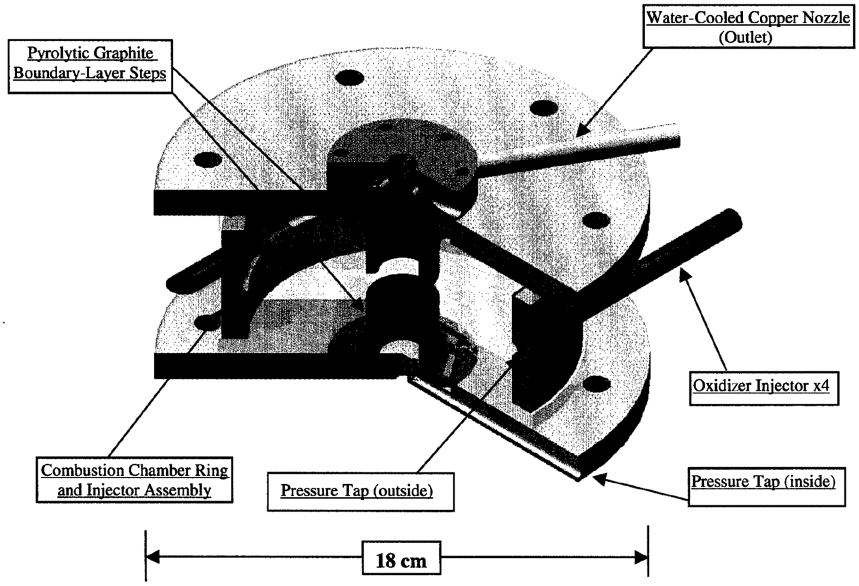

Fig. 2 Surrey Satellite Technology pancake hybrid motor [15].

fuel grain. These internal flowpaths allow for motor aspect ratios that are significantly shorter than can be achieved using conventional solid, hybrid, or monopropellant technologies. These flowpaths cannot be achieved with thermosetting materials that are cast using tooling, which must be removed once the material is set. The similarity in burn performance of ABS to HTPB allows FDM to be used in the manufacturing of fuel grains with little or no performance penalty.

C. Design and Development of the Helical MUPHyN Fuel Grain

Surrey Satellite Technology has previously developed a compact hybrid motor concept, a "pancake" hybrid, in 2001 [15]. Figure 2 shows the pancake design with tangential injection on the exterior of the short motor casing. They demonstrated relatively high combustion efficiencies compared with standard hybrid motor designs, a feature they attributed to centrifugal forces keeping unburned pieces of fuel away from the nozzle exit in the center of the motor.

Knuth et al., at Orbital Technologies Corporation (OrbiTech), designed a "vortex hybrid" motor [16]. Their design uses tangential injection that is balanced such that coaxial vortexes form in the motor port. Figure 3 shows the motor design featuring the vortex flowpath. These coaxial vortices increase the effective oxidizer mass flux near the fuel surface, increasing regression, and the center vortex provides ample time for mixing and combustion. This design showed high regression rates with traditional rubber fuels, as well as high combustion efficiencies similar to the pancake design.

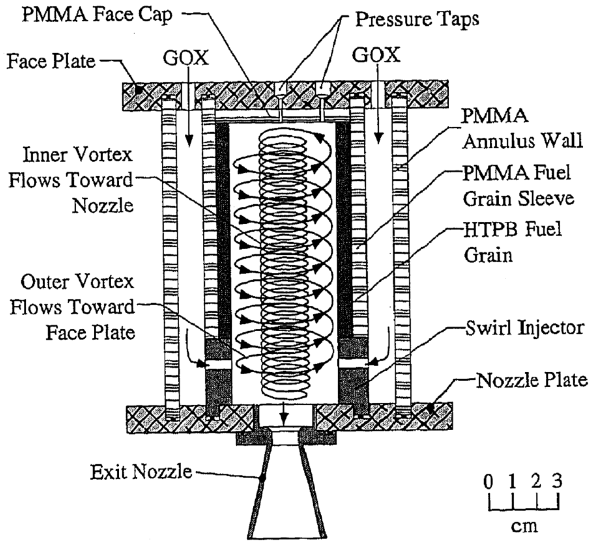

Fig. 3 Pennsylvania State University "vortex injection" hybrid motor [16].

The MUPHyN design is similar to the pancake hybrid in form factor, but moves the injectors on the outside of the case to the inside, allowing for the easy incorporation of an aerospike nozzle in the center of the motor and the incorporation of regenerative cooling for the inner side of the aerospike throat. This design feature allows for the potential marriage of a form factor applicable to small satellites, as well as the combustion efficiency gains of vortex and pancake hybrids with the volumetric and performance benefits of aerospike nozzles.

For the MUPHyN motor, the ability to manufacture complex grain designs is a critical enabling technology. The "vortex" design of the OrbiTech motor [16] was adapted to the MUPHyN thruster by embedding a helical fuel port inside of the fuel grain. This helical port structure is enabled using FDM to fabricate the ABS fuel grain module with the embedded helical port. This embedded helical port provides an extended length flowpath large-surface contact area in a short form factor, analogous to that demonstrated by the vortex hybrid. The centrifugal forces created by the combustion gases rotating in the helix core significantly increase the fuel regression rates and propellant mass flow. This design feature produces sufficient total fuel mass flow so that the total oxidizer-to-fuel ratio remains low enough to prevent nozzle erosion during the entire motor burn.

D. Nonpyrotechnic, Multiple-Use, Inductive-Discharge Igniter for MUPHyN Thruster

To mature the final key feature of the MUPHyN thruster design, a parallel development activity at USU has produced a prototype gas-generation ignition system that uses a low-energy, high-voltage inductive spark to ignite a hydrocarbon-based fuel like ABS or HTPB in gaseous oxygen. The developed gas-generation system allows for multiple restarts with a single hydrocarbon fuel grain and is effectively a small hybrid-rocket motor. The design alleviates safety issues associated with bipropellant ignition sources and circumvents the disadvantages of single-use small solid-propellant igniters. Figure 4a shows an exploded view of the prototype igniter design. Figure 4b shows the solid-fuel igniter being pulsed. The prototype igniter is constructed with an acrylic pressure case so that the electrical discharges can be seen externally. The number of restarts possible with this igniter is only limited by the amount of solid fuel in the igniter. To date, tests have been conducted showing up to 27 ignitions of the prototype igniter on the same fuel grain.

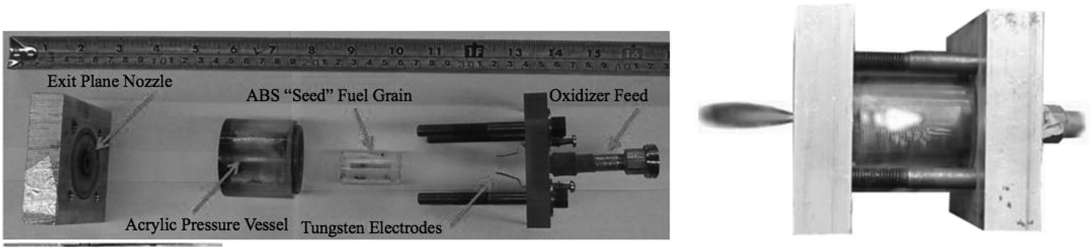

a) Exploded view b) Prototype ignitor being test fired

Fig. 4 Prototype electrical-discharge solid-fuel ignition system.

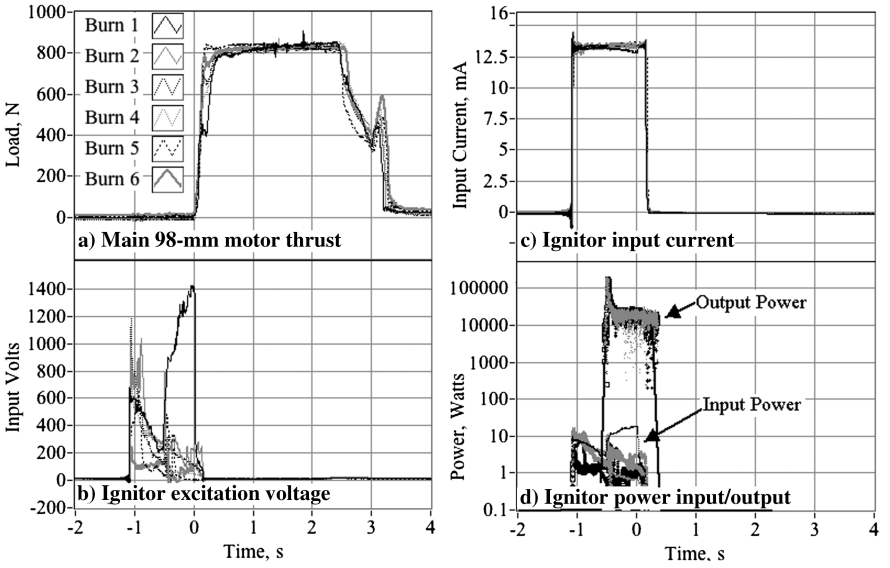

Fig. 5 Ignition tests of 98-mm-diam hybrid motor with prototype electrical-discharge ignition system.

The proof-of-concept prototype igniter design successfully ignited a 98 mm nitrous oxide/HTPB hybrid-rocket motor multiple consecutive times without changeover [17]. For initial proof-of-concept tests, the high-voltage spark was provided using a handheld stun gun that could achieve multiple ignitions on a single charge of a 30 g, 0.25 Ah, 4.8 V lithium-ion battery. Later tests used a precision high-voltage power supply with a current limiter. Figure 5 plots typical results from the successive ignition tests. The required power input started at less than 10 W for the initial burn, and then dropped to 2 W for the final burn. Total burn input energies averaged less than 5 J. The gas byproducts from the hydrocarbon-seeding process exceeded 2200 C with an output enthalpy rate of greater than 25 kW. For these tests, the igniter burn time overlapped main motor ignition by approximately 100–200 ms. The mean total output energy for the igniter burns exceeded 20 kJ.

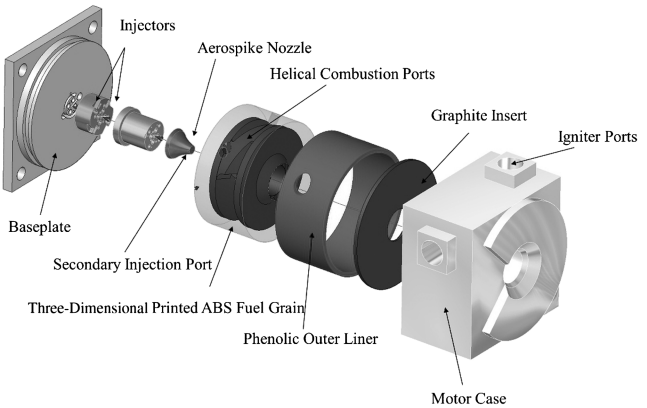

Fig. 6 Exploded view of prototype MUPHyN thruster assembly.

IV. Prototype MUPHyN Thruster: Design Details

Figure 6 shows an exploded view of the prototype MUPHyN thruster assembly and summarizes the primary design parameters. This prototype article was used to perform the ground tests to be described in the following sections of this paper. This prototype MUPHyN thruster design includes an FDM-manufactured fuel grain with an embedded helical fuel port and an annular aerospike nozzle held by a central injector support fixture. The motor case is designed to fit within a 1U section of the cubesat bus.

The aerospike nozzle contour was designed using the method of characteristics technique developed by Lee and Thompson [18]. The design nozzle expansion ratio is 2.25:1 and was selected as a compromise between performance, manufacturability, and heat transfer considerations that will be discussed in Sec. IV.B. The 2.25:1 expansion ratio results in a nozzle that is slightly over-expanded for the ambient pressure conditions at the test location in Logan, Utah, approximately 1300 m above mean sea level. The nozzle was truncated at 70% of its theoretical length. The 70% nozzle truncation results in a 4% decrease in the theoretical thrust-level produced in optimally or overexpanded flow conditions [19]. However, this truncation substantially enhances the manufacturability of the nozzle contour. Thus, the performance loss resulting from the 70% truncation is accepted as a design compromise. For a higher performance nozzle configuration, this loss could be compensated by base bleed [20].

The inner throat and nozzle plug are regeneratively cooled and the outer throat is constructed from high-density graphite. Nitrous oxide (the oxidizer) flows through the base of the MUPHyN, to the throat, and then down and out the tangential injectors into the combustion chamber. Figure 7 shows the oxidizer/coolant flowpath. The walls of the combustion chamber are insulated with a phenolic liner on the sides and a graphite insert on the top (downstream near the nozzle

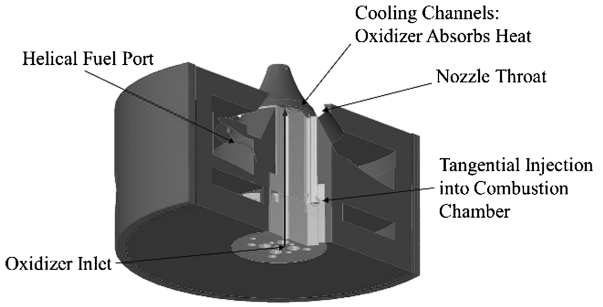

Fig. 7 MUPHyN coolant flowpath.

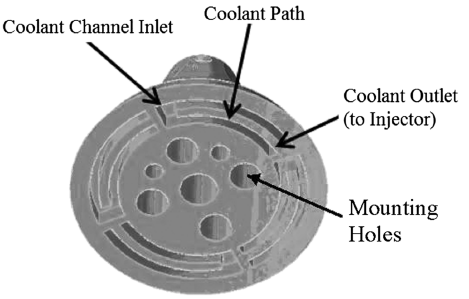

Fig. 8 Aerospike nozzle coolant flow channels on bottom of aerospike nozzle.

exit). The outer casing of the test article is manufactured out of medium carbon steel. The base of the motor case is aluminum and the aerospike components are copper to support heat transfer to the oxidizer. The prototype test article included a single secondary injection port to allow the effectiveness of secondary injection thrust vectoring to be evaluated for hot-fire test conditions. The injection orifice is located near the end of the aerospike nozzle, which was shown to have the highest efficiency in previous cold-flow tests [21].

A. Regenerative Cooling System Design Features

A recurring problem with aerospike nozzle designs is managing the high thermal load imparted to the nozzle by the combustion products around the small annular throat exit gap. Aerospike nozzles with high expansion ratios have a far larger throat surface area than a bell or conical nozzle with the same throat exit area, and imparted heat loads are significantly higher. Fortunately, the compact design of the MUPHyN thruster allows for relatively straightforward application of regenerative cooling using the oxidizer flow.

The MUPHyN coolant system design is derived from research performed by Lemieux et al. at California Polytechnic State University, where nitrous oxide was used to cool a copper-throated conical nozzle [22,23] and was later designed to cool an aerospike nozzle in a traditionally long form hybrid motor [24]. The authors found that saturated nitrous oxide (when care is taken not to allow the liquid phase to fully boil off) is an effective regenerative coolant. If the liquid phase is allowed to fully boil off, heat transfer to the coolant reduces significantly. If heat transfer is high enough, the resulting vapor could reach temperatures that would support exothermic decomposition, an event that could produce catastrophic failure of the aerospike nozzle.

The MUPHyN motor shape, with its compact longitudinal form factor, allows oxidizer to be passed through coolant channels near the throat and then back down to an injector near the bottom of the combustion chamber with no external plumbing. Figure 8 shows the cooling channels on the MUPHyN nozzle.

B. Analysis of the Convective Heat Transfer from the Combustion Flame Zone to the Aerospike Nozzle

Convective heat transfer from the nozzle flowfield to the nozzle surface in traditional deLaval rocket nozzles is generally predicted with correlations derived for fully developed pipe flow [7]. Convective heat transfer in an aerospike nozzle is not fully developed and the axisymmetric model developed by Mayer [25] for external expansion, spike, and other novel rocket nozzle configurations is more applicable. Instead of a hydraulic diameter-based correlation, the model created by Mayer uses a thermal Reynolds number of the form

$$Re_\Gamma = \frac{\rho_\infty U_\infty \Gamma}{\mu_\infty} \tag{1}$$

where Γ is the thermal boundary-layer thickness. Assuming a control volume inside this thermal boundary layer, an energy balance yields

$$q_w = \mu_\infty \bar{c}_p T_{0,\infty} \frac{\mathrm{d}}{\mathrm{d}s} Re_\Gamma \tag{2}$$

where ds is the curvilinear differential length. A modified form of the Reynolds analogy correlation,

$$St_\infty = BPr_\infty^{-\frac{2}{3}} Re_{x,\infty}^{-b} \tag{3}$$

is applied to relate the thermal Reynolds number to the traditional fluid-dynamic Reynolds number:

$$Re_{x,\infty} = \int_0^s \frac{\rho_\infty U_\infty}{\mu_\infty}\,\mathrm{d}s \tag{4}$$

In Eqs. (3) and (4), St_∞ is the Stanton number, B and b are empirical constants, and Pr is the Prandtl number of the core oxidizer flow. The heat transfer coefficient H is expressed in terms of the integral

$$H_2(s) = \rho_\infty \bar{c}_p U_\infty St = \frac{\beta^{(1/(1-b))} BPr^{-(2/3)} \rho_\infty \bar{c}_p U_\infty}{[\int_0^s \beta^{(1/(1-b))} \rho_\infty \bar{c}_p U_\infty \mu_\infty^{-1}]^b} \tag{5}$$

where the parameters in Eq. (5) are defined as [25]

$$\beta = \left(\frac{T_{\mathrm{surf}}}{T_*}\right)^{(1-b(1+\omega))} \qquad B = 0.0296 \quad b = \frac{1}{5} \quad \omega = \frac{3}{2} \tag{6}$$

Equation (5) is corrected for annular surfaces to yield the relationship

$$H_3(s) = H_2(s)\left[\frac{r^{(1/1-b)} \int_0^s \beta^{(1/(1-b))} \rho_\infty \bar{c}_p U_\infty \mu_\infty^{-1}}{\int_0^s (\beta r)^{(1/(1-b))} \rho_\infty \bar{c}_p U_\infty \mu_\infty^{-1}}\right]^b \tag{7}$$

Table 3 lists combustion and nozzle parameters used to calculate fluid properties for this model. The combustion products were computed with the NASA code Chemical Equilibrium Analysis with Applications [26,27].

For this analysis, a uniform aerospike surface temperature of 400 K was assumed. Although the actual surface temperature will vary with both heat transfer rate and location, this surface variation should be small compared with the difference between the surface temperature and the far higher combustion gas flame temperature. This effect is expected to be much lower than the general accuracy of this model and is thus neglected. The local mean cross section combustion gas

Table 3 MUPHyN motor combustion and nozzle parameters

Parameter	Value
Outer throat radius	1.2 cm
Chamber pressure	775.6 kPa
Specific heat ratio	1.27
Molecular weight	24.247
Expansion ratio	2.25
Viscosity	0.844 mP
Chamber temperature	3046 K
Viscosity temperature exponent	1.5
Convergent surface length	0.75 cm
Aerospike surface temperature	400 K

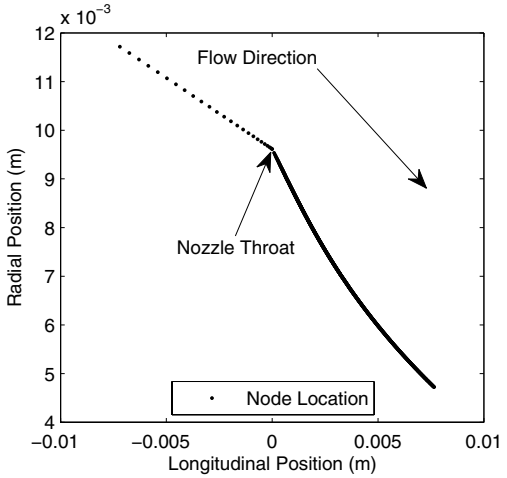

Fig. 9 Geometry and node locations used for hot-side convective heat transfer calculations.

temperature $[T(s)]$, pressure $[P(s)]$, and sonic velocity $[U(s)]$ were calculated using local isentropic flow relationships:

$$T(s) = \frac{T_0}{(1+\frac{1}{2}(\gamma-1)M(s)^2)}$$
$$P(s) = \frac{P_0}{(1+\frac{1}{2}(\gamma-1)M(s)^2)^{(\gamma/(\gamma-1))}}$$
$$U(s) = M(s)\sqrt{\gamma R_g T(s)} \tag{8}$$

The convective heat transfer to the nozzle was calculated by breaking the surface into a series of local nodes. A 0.75 cm convergent section was chosen to model boundary-layer growth before the throat. Cosine clustering toward the throat was used to place nodes along the convergent section and the nodes created by a method of characteristics solver were used for the divergent section. This geometry is shown in Fig. 9. Conical frustum areas between nodes and trapezoidal integration were used for surface integration of total heat transfer rates. Because of the significantly lower surface heating rates, the base region was not included in this analysis. Figure 10 plots the resulting convective heat transfer coefficients and area-specific heat transfer rates. The resultant total heat transfer computed via this method is about 3500 W.

As noted previously, the low expansion ratio of 2.25:1 on the prototype MUPHyN was significantly lower than would be desirable for a space thruster. Assuming a fixed throat area (and exit mass flow) for an aerospike nozzle, the exposed surface area increases proportionately with nozzle expansion ratio. A high expansion ratio

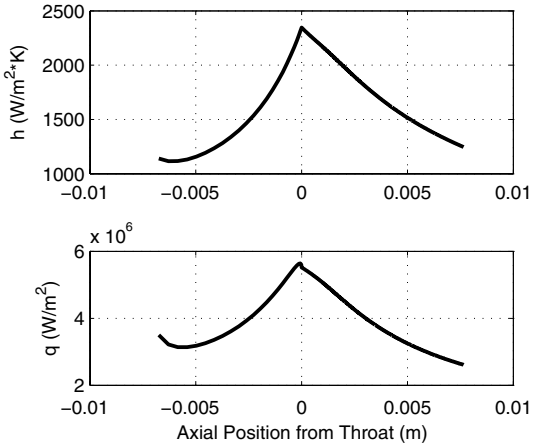

Fig. 10 Heat transfer coefficient and heat transfer rate for aerospike surface.

nozzle will experience a significantly higher convective heating load than will a low expansion ration nozzle. Thus, the low expansion ratio of the MUPHyN prototype was selected to allow a significant heating margin of safety for the preliminary rounds of testing. Once the precise convective heating levels are better understood, future MUPHyN development tests will scale the expansion ratio upward to be more efficient for vacuum operation.

C. Analysis of the Regenerative Cooling Nitrous Oxide Heat Transfer Rate

As shown in Fig. 11, nitrous oxide flow through the cooling channels in the MUPHyN configuration can be broken down into four fluid states. Nitrous oxide enters the MUPHyN motor regenerative cooling paths in liquid form at slightly above saturation pressure. As the fluid enters the cooling channels, it encounters a constrictive orifice that expands the flow to a significantly lower pressure. This expansion is assumed to be adiabatic because the expansion orifice is located before the heat transfer channels. Between states 2 and 3, external energy is added through heat transfer from the external combustor flow and, finally, at the injector (state 4), the multiphase fluid adiabatically expands to the combustor chamber pressure.

The coolant side heat transfer can be modeled with relations originally developed for boiling in smooth circular tubes [28,29]. Although, as can be clearly seen in Fig. 8, the coolant channels in the MUPHyN are not circular tubes, the flow in the impinging jet channels with fins should facilitate even higher heat transfer. Thus, it is believed that this will yield a conservative estimate.

Nitrous oxide is expanded through an orifice to state 2 as shown in Fig. 11. This expansion drops the fluid pressure below the initial saturation pressure. This results in multiphase heat transfer. Because the phase change removes significantly more heat than convection to liquid flow alone, the multiphase heat transfer is expressed as in terms of a ratio relative to liquid heat transfer alone [28,29]:

$$\frac{H}{H_l} = 0.6683\left(\frac{\rho_l}{\rho_v}\right)^{0.1} X^{0.16}(1-X)^{0.64} f(Fr) + 1058\left(\frac{q''}{\dot{m}'' h_{fg}}\right)^{0.7}(1-X)^{0.8} G_{s,f} \tag{9}$$

$$\frac{H}{H_l} = 1.136\left(\frac{\rho_l}{\rho_v}\right)^{0.45} X^{0.72}(1-X)^{0.08} f(Fr) + 667.2\left(\frac{q''}{\dot{m}'' h_{fg}}\right)^{0.7}(1-X)^{0.8} G_{s,f} \tag{10}$$

In Eq. (9), $\dot{m}$" is the total mass flow through the channel divided by the channel area, and the term G is a constant related to the specific materials and coolants used, but generally ranges around 1.0. The stratification parameter $f(Fr)$ accounts for stratification that can develop in long horizontal tubes and is equal to unity for vertical channels. As the channels in the MUPHyN are neither long nor horizontal, this parameter was also assumed to be unity. The coefficients in these relationships were empirically obtained [28]. Equation (9) models heat transfer for convective dominated flow regimes, and Eq. (10) models heat transfer in nucleate boiling regimes. The larger of the two values determines which effect

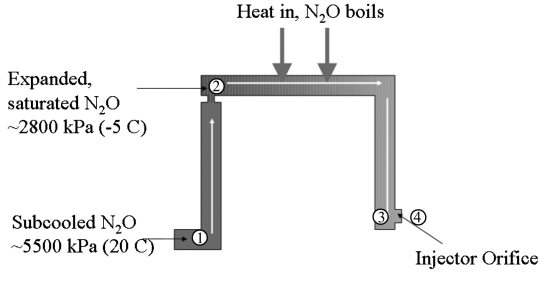

Fig. 11 Nitrous oxide coolant flow and states.

Table 4 Boiling heat transfer parameters

Parameter	Value
Specific heat transfer rate, q''	7430 kW/m^2
Total heat transfer rate	3500 W
Mass flow rate	0.08 kg/s (total)

dominates and, therefore, which relationship should be used. Table 4 lists the other relevant parameters used in this calculation. For this analysis the total heat transfer rate is calculated using the convective and regenerative cool calculation as presented by Secs. IV.B and IV.C. Fluid-specific properties were computed using Helmholtz relations for real fluids [30–32].

State properties for nitrous oxide at different coolant pressures were calculated assuming isenthalpic expansion across the orifice before the coolant channels. Any heat transfer to the fluid was assumed to happen after this initial expansion. Depending on coolant pressure, the ratio of multiphase heat transfer to liquid only heat transfer ranges between 10 and 20 for this configuration.

To complete the heat transfer model, a liquid-phase heat transfer relationship is required. The liquid heat transfer coefficient is modeled by [7,29]

$$H_l = 0.023 c_{p_l} \frac{\dot{m}}{A} \left(\frac{DU\rho_l}{\mu_l}\right)^{-0.2} \left(\frac{\mu_l C_{p_l}}{\kappa_l}\right)^{-(2/3)} \tag{11}$$

where $\dot{m}$ is the total fluid flow rate. Figure 12 plots the heat transfer coefficients computed using this method for a range of coolant pressures, along with the average fluid quality. Figure 13 plots the predicted nozzle surface temperatures, along with the nitrous oxide temperatures.

D. Nonhomogeneous Nonequilibrium Two-Phase Mass Flow Model

A modified version of the nonhomogeneous nonequilibrium (NHNE) model developed by Dyer et al. at Stanford University was used for injector size calculation [33]. This model uses a weighted average of the homogeneous equilibrium (HEM) mass flux,

$$G_{\text{HEM}} = \frac{\dot{m}}{A} = \rho_2 \sqrt{2(h_1 - h_2)} \tag{12}$$

and the incompressible mass flux (SPI),

$$G_{\text{SPI}} = \frac{\dot{m}}{A} = \sqrt{2\rho_1 (P_1 - P_2)} \tag{13}$$

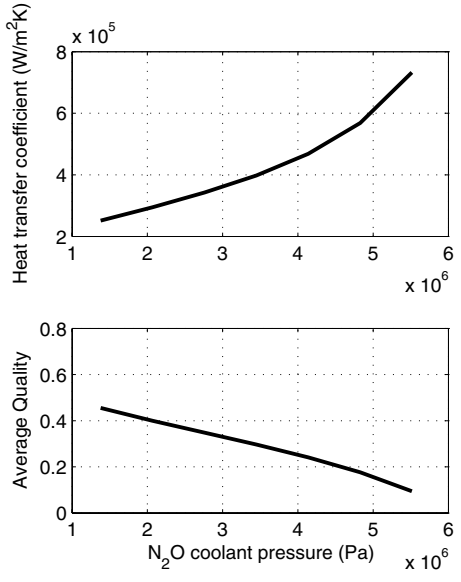

Fig. 12 Coolant side heat transfer coefficient and average coolant quality.

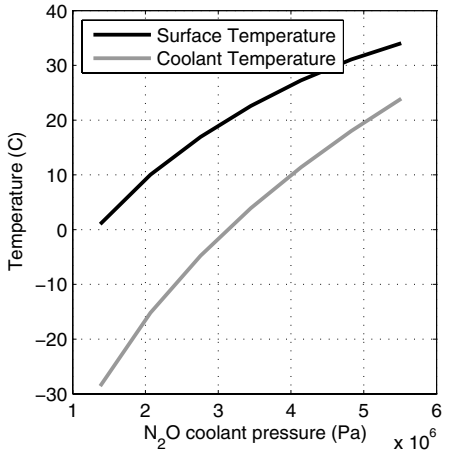

Fig. 13 Coolant side aerospike surface and coolant temperature for heat transfer of 3500 W.

to compute a single mass flux using a weighted "nonequilibrium parameter" k,

$$k = \frac{\tau_b}{\tau_r} = \sqrt{\frac{P_1 - P_2}{P_v - P_2}} \tag{14}$$

The two-phase mass flux is calculated as a weighted average of the incompressible and HEM mass fluxes,**

$$G_{\text{NHNE}} = C_d \left(\frac{1}{1+k} G_{\text{HEM}} + \left(1 - \frac{1}{1+k}\right) G_{\text{SPI}} \right) \tag{15}$$

In these relations, the subscript 1 represents the conditions at the orifice inlet, and the subscript 2 represents the conditions at the outlet. This same relationship, with different pressure drops and initial qualities, applies to both the expansion orifice positioned before the coolant channels and the injector orifice that sprays into the combustion chamber.

The parameter k is the inverse square root of the Cavitation number and expresses the ratio of the difference between the upstream total pressure and the downstream pressure, and the vapor pressure and the downstream pressure. Small values for k demonstrate a high degree of cavitation in the flow and an increase in fluid quality in the injector orifice. When k is large, the incompressible SPI model is weighted heavily. When k is small, the two-phase HEM model is weighted heavily. The combined model of Eq. (15) allows for two-phase flow effects that plateau the mass flux as the downstream pressure is lowered. This is consistent with observed two-phase mass flow properties.

The model proposed by Dyer et al. [33] was further extended to incorporate choking mass flow. For very small exit pressures, the mass fluxes predicted by the NHNE model decrease with decreasing exit pressure, a trend unlikely to exist in reality. Thus, a model was used that uses the maximum flow rate predicted by the NHNE model for any downstream pressure between the upstream pressure and the exit pressure. Figure 14 shows mass fluxes predicted by the SPI model, the HEM, the NHNE model, and the choked NHNE model (CNHNE) for nitrous that is slightly subcooled upstream of the injector. It is noteworthy that the SPI model and HEM are identical if the downstream fluid is still subcooled, and the CNHNE and NHNE model are identical above about 1 MPa.

E. Injector and Expansion Orifice Size Calculation

To maintain the desired coolant pressure and mass flow rates, the orifice before the coolant channels, as well as the injector orifice,

**It should be notes that [33], erroneously interchanges the G_{HEM} and G_{SPI} terms. This reversal of terms lead to a mass flux tending towards G_{HEM} when vapor pressure is becomes low, a scenario that is not physically possible.

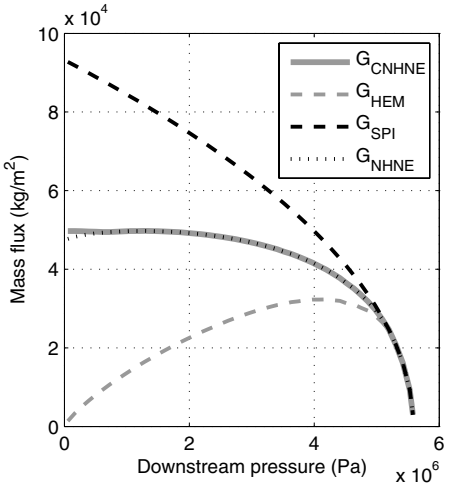

Fig. 14 Predicted Mass-flux as function of downstream pressure at 5.58 MPa upstream pressure.

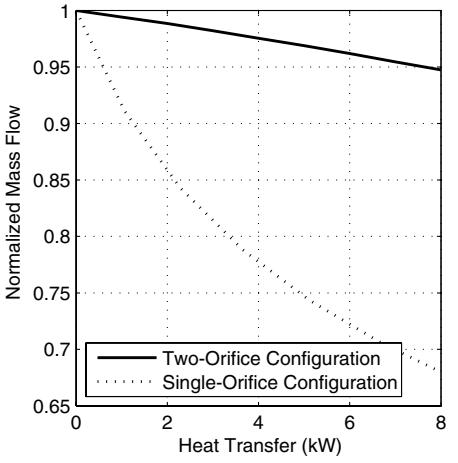

Fig. 15 Mass flow rate variation with heat transfer into oxidizer flow for single and double pressure drop configurations.

must be correctly sized. Clearly, increasing the pressure drop across the initial orifice decreases the pressure and, therefore, the fluid temperature in the coolant channels. Also, reducing the coolant pressure increases the fluid vapor-to-liquid ratio (quality) of the fluid in the coolant channels. This increase in fluid quality significantly decreases the overall heat transfer coefficient. If this were the only parameter of interest, it would therefore be desirable to maximize the heat transfer coefficient by minimizing the coolant quality. However, heat transfer into the fluid along the regenerative cooling channels can significantly influence the exit fluid state properties (including density) and will significantly affect the mass flow rate into the motor. Thus, it is desirable to have a large pressure drop before the coolant channels. This pressure drop at least partially chokes the oxidizer flow, and has the effect of decoupling the mass flow rate through the system from the nozzle plug regenerative heat transfer rate into the flow. Figure 15 compares the variation of mass flow rate as a function of heat transfer rate to the fluid for a single orifice configuration, and a two-orifice configuration that produces a large pressure drop just upstream of the coolant channels. The effect of the second choking orifice in clearly evident. The mass flow rate is normalized using the calculated CNHNE mass flow with no regenerative cooling. Hence, this pressure drop has the effect of decoupling the total mass flow rate from the heat transfer into the fluid. If the fluid mass flow rate was significantly affected by the amount of regenerative heat transfer and the orifice sizes were designed for the steady-state operational condition, a substantially higher mass flow rate would exist during the start up transient. This could result in a potential combustion chamber over pressurization during the startup thermal transient for the motor.

For this system, the run lengths are very short and the coolant channel diameters are much larger than the expansion and injection orifices. Thus, the pressure drops should be dominated by these expansions. Therefore, it is desirable to pick orifice sizes between states 1 and 2, and also between states 3 and 4, such that the total mass flow rate is 0.08 kg/s and the pressure at states 2 and 3 is 2760 kPa

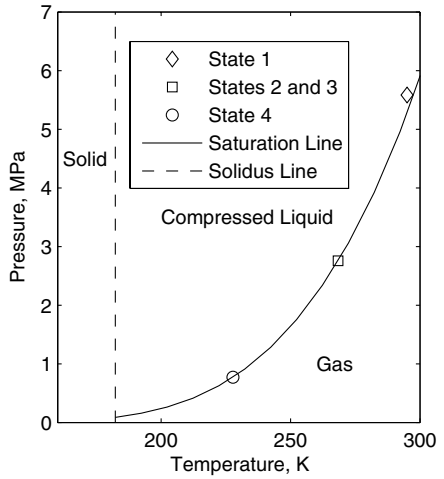

Fig. 16 Nitrous oxide coolant states on nitrous oxide phase diagram.

(400 psi). Pertinent fluid parameters are listed in Table 5 based upon isenthalpic expansion described earlier and 3500 W of heat addition between states 2 and 3. An incompressible discharge coefficient of 0.85 was assumed for this analysis. This should be a reasonable number for square-edged orifices.

To achieve the design thrust level of 125 N for the prototype MUPHyN thruster, the injection and throttling orifices (the orifices between states 1 and 2, and 3 and 4, respectively) were sized to achieve a mass flow rate of approximately 0.08 kg/s with a oxidizer inlet pressure approximately 5500 kPa. The resulting the pressure is approximately 2750 kPa for each of four coolant channels, and the design chamber pressure is approximately 690 kPa. Tables 5 and 6 show the corresponding fluid properties and coolant flux rates at each

Table 5 Nitrous oxide coolant states

State	Fluid temperature, K	Pressure	Quality	Total density, kg/m^3	Total enthalpy, kJ/Kg	Total entropy, kJ/Kg · K
1	295	5590 kPa (810 psia)	0	770	218	0.890
2	268	2760 kPa (400 psia)	0.26	232	218	0.913
3	268	2760 kPa (400 psia)	0.44	153	262	1.07
4	228	772 kPa (112 psia)	0.58	34.1	262	1.18

Table 6 Nitrous oxide coolant states

Orifice	G, kg/m^2 · s	G_{HEM}, kg/m^2 · s	G_{SPI}, kg/m^2 · s	Total area required, E-6 m^2	Chosen orifice diameter, mm
1–2	39,840	27,741	66,035	2.008	0.8 (1/32 drill)
3–4	14,460	8,739	25,283	5.533	1.3 (#55 drill)

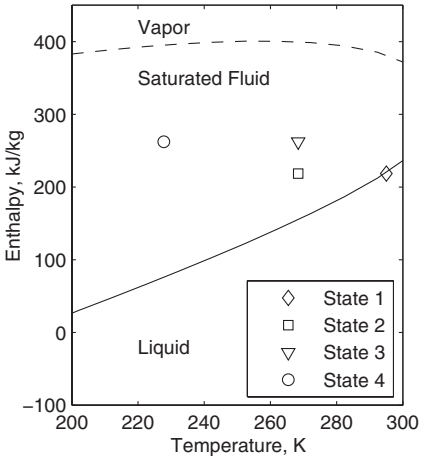

Fig. 17 Nitrous oxide coolant states on nitrous oxide temperature-enthalpy diagram.

of the state points 1–4. These states are also shown on the phase diagram for nitrous oxide [34] in Fig. 16 and on the temperature-enthalpy diagram in Fig. 17. Figure 15 illustrates the change in mass flow rate with heat transfer for this configuration and a configuration with heat transfer into the fluid before a single pressure drop into the combustion chamber. At the design operating condition of about 3500 W of heat transfer, the two-orifice configuration described earlier will have a flow rate about 2% below that without heat transfer. If there was not a stabilizing initial pressure drop, the total mass flow rate would drop by nearly 21% once steady-state heat transfer was reached.

V. Experimental Apparatus Used for MUPHyN Tests

The MUPHyN hot-fire static tests used an existing test stand modified to accomplish the MUPHyN test objectives. This system features a the Mobile Nitrous Oxide Supply and Test Resource (MONSTER) cart that contains a run tank, which is preloaded with nitrous oxide from three "k-sized" bottles with dip tubes. The run tank is then top pressured with helium for the duration of the burn. Carbon dioxide is used to purge the system after a burn. Figure 18 shows the piping and instrumentation diagram for the MONSTER cart oxidizer delivery system. Primary flow is controlled via a binary pneumatic-operated ball valve and secondary flow is controlled via a fast-response solenoid valve.

A custom-designed Venturi flow meter measures primary oxidizer flow and another similar but smaller Venturi is used to measure the flow rate of the thrust-vectoring fluid. For these measurements, the Venturi discharge coefficient was assumed equal to the high Reynolds number value of 0.985. From laboratory calibration and testing, the estimated 95% confidence interval for these meters is approximately ±0.5% of the indicated flow rate.

To measure both axial thrust and side force, a 4 degree-of-freedom (DOF) thrust balance was designed specifically for MUPHyN testing. Two axial load cells are used to measure axial thrust and a two-side load cell measures the much smaller side forces as well as axial torque. The test stand features custom-engineered three axis flexures in the vertical and axial directions to limit frictional load losses and ball-and-clevis joints on the side load cells. Figure 19 shows the MUPHyN thruster mounted in the 4-DOF test stand. The axial load cells on the MUPHyN test stand were calibrated using conventional single-axis methods, assuming a linear model with a bias. However, the test stand was calibrated for side force, roll, and yaw using a simultaneously multivariable calibration method similar to the one previously described by Eilers et al. [13]. The method was modified from that cited earlier to allow drift of the bias during calibration, whereas the previous method assumed zeroed reference data. The resulting side-force calibration has a 95% uncertainty interval of approximately ±0.038 N or about ±0.5% of the nominal side-force value.

VI. Hot-Fire Test Results

A total of seven hot-fire static tests have been performed on the MUPHyN prototype: six "successful" test fires and an

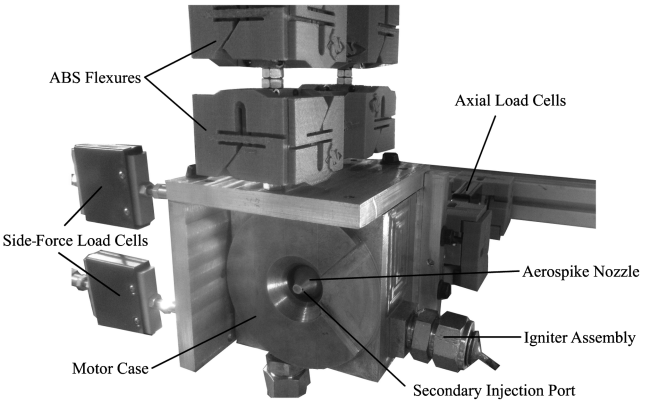

Fig. 19 MUPHyN assembly mounted in 4-DOF thrust stand.

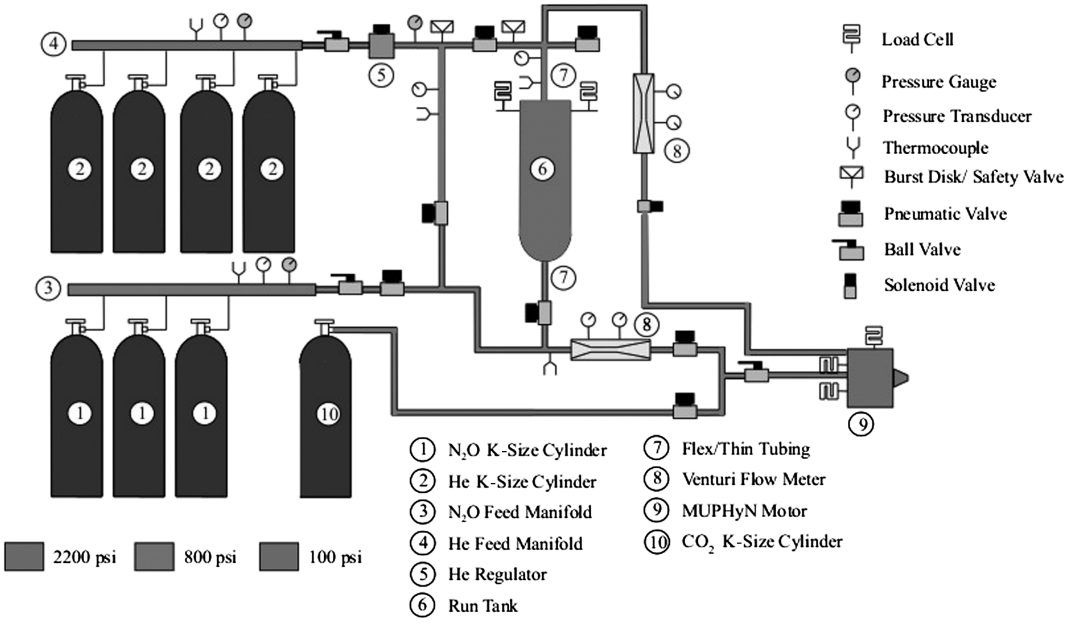

Fig. 18 Plumbing and instrumentation diagram for "MONSTER cart" supply system.

Table 7 MUPHyN test fire summary

Test no.	Burn time, s	I_{sp}, s	Total impulse, ns	Characteristic velocity, m/s	O/F ratio	Secondary injectant	Mean oxidizer flow rate, kg/s
HF1	3	137	487	1367	3.16	None	0.088
HF2	3	122	370	na	4.14	Helium	0.077
HF4	3	128	400	1325	3.13	Helium	0.077
HF5	3	106	320	1195	3.16	Nitrogen	0.072
HF6	4	144	450	1473	3.35	Nitrogen	0.060
HF7	4	142	469	1451	3.38	Oxygen	0.063
Measurement uncertainty, 95%	— —	±2.4%	±0.4%	±3.4%	±1.5%	— —	±0.05%

instrumentation system checkout hot fire. Table 7 summarizes these tests.

A. Primary Plenum Flow Test Results

Figure 20 presents pressure and thrust time-history profiles for a typical MUPHyN burn. After the initial startup transient, the motor achieves a steady-state thrust level that is within 5% of the design value of 120 N. Obviously, the I_{sp} values listed in Table 7 are significantly lower than would be expected for a well-tuned hybrid-rocket motor. Additionally, the characteristic velocities are far below those expected for this fuel combination. For comparison, tests completed with nitrous oxide and HTPB at USU in a traditional hybrid motor yielded specific impulses of about 195 s with an expansion ratio of 4.514 and an average characteristic velocity of about 1450 m/s. There are two major potential contributors to this lowered performance: 1) This initial series of tests was designed to have a higher than desirable oxidizer mass flow rate of oxidizer to ensure sufficient cooling, and 2) the fuel regression rate was much higher than initially anticipated. The high total mass flow rates result in very low chamber dwell times, potentially lowering combustion efficiency. The high regression rates also decreased the O/F ratio well below optimum for many of the tests, also decreasing overall performance. The high regression rate is presumably due to centrifugal flow effects produced by the helical port in the ABS fuel grains. Although the high regression rate is not by itself undesirable, the lower O/F ratio tends to both decrease the performance directly and lower the flame temperature. As noticed by Strand et al., a decrease in the flame temperature could lower the rate of chemical kinetics, yielding lower flame temperatures and efficiencies in a viscous-circle-type process [35]. It should be noted that the later fuel grains were designed to increase mixing, and these fuel grains do indeed show a substantial increase in characteristic velocity. Figure 21 contains photographs of each of the burned fuel grains for each of the test fires listed in Table 7.

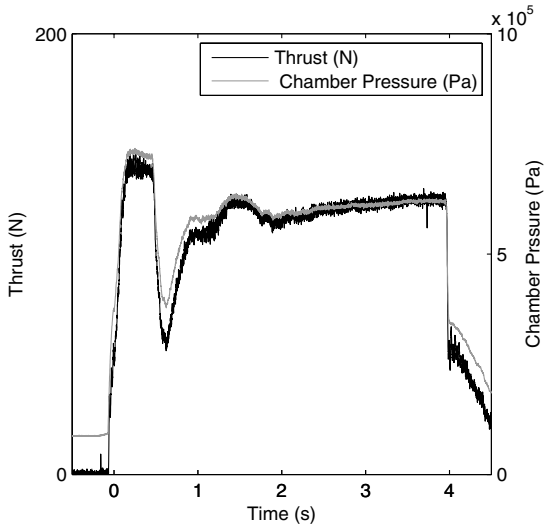

Fig. 20 Typical thrust and chamber pressure traces for MUPHyN hot fires.

B. Regenerative Cooling Test Results

During each of the MUPHyN test firings, there was no notable erosion on the aerospike surface, and the regenerative cooling system maintained the aerospike and the supporting injector structure well within material temperature limits. The combustion flame temperature is estimated to exceed 2800 C.

Figure 22 presents temperature profiles from two hot-fire tests performed with an Omega type-K thermocouple embedded just inside of the nozzle coolant channels. The location of this thermocouple in relation to the coolant channels is shown in Fig. 23. A large nozzle temperature difference between the two tests is noted. The initial MUPHyN tests used a graphite insulator below the aerospike nozzle. In later tests, this insert was replaced with ABS fuel, which substantially lowered the total heat transfer into the fuel grain. Heat transfer through the graphite insert was neglected for the heat transfer analysis, which may be the source of the underpredicted nozzle temperature.

For the tests with ABS insulation, the aerospike temperature presented in Fig. 22 shows reasonable agreement with the predicted aerospike temperature discussed earlier and shown in Fig. 13 for a net heat flux of about 3500 W. This result suggests that the heat transfer models used in this analysis are a reasonable approximation.

C. Effects of Fuel Grain Geometry on Fuel Regression Rate and Motor Performance

Using typical skin-friction-based hybrid motor regression-rate prediction models [36], the average regression rates in the MUPHyN motor were expected to be near 1.0 mm/s and the chamber ports/test fire durations were designed such that it would require over twice this

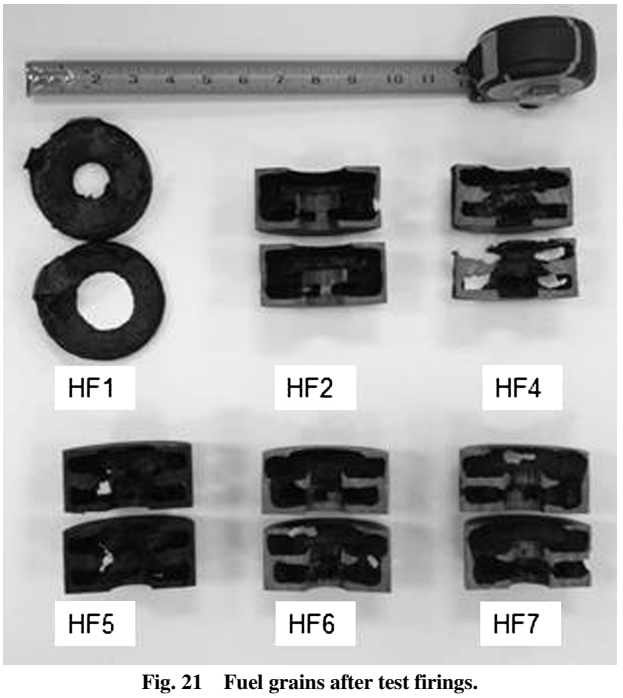

Fig. 21 Fuel grains after test firings.

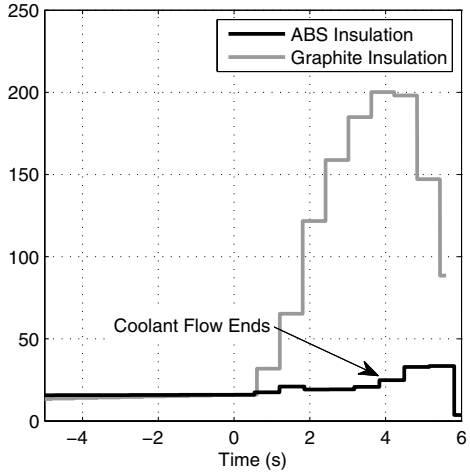

Fig. 22 Aerospike nozzle temperature for both ABS- and graphite-insulated center plug. Time = 0 corresponds to motor ignition.

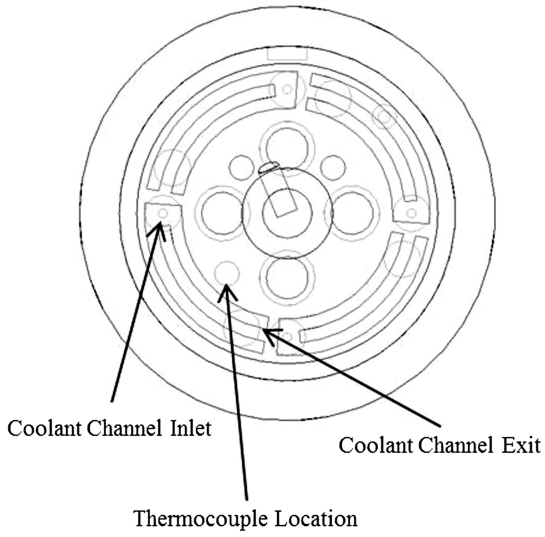

Fig. 23 Thermocouple location relative to coolant channels.

regression rate to burn through the 6.6 mm fuel port wall during a motor firing. As seen in Fig. 21, the original MUPHyN helix demonstrated much higher fuel regression rates than expected (at least 2.0 mm/s, as evidenced by regression completely through the fuel grain walls) and low combustion efficiencies (as seen by the low specific impulses). In addition, the oxidizer flow rate was constrained by requirements to maintain a high safety factor on coolant capacity, not thrust level or desired oxidizer mass flux. The test HF5 showed ample cooling capacity once the center aerospike support was insulated with ABS instead of graphite. This allowed more flexibility in nitrous oxide flow rates. For the next two tests, the main oxidizer flow rate was decreased by approximately 25%, which allowed for lower oxidizer mass fluxes in the fuel grain. This, in turn, allowed for greater flexibility in fuel grain design.

For HF6 and HF7, the double-helix design was replaced with a triple-helix design with much thinner and taller combustion chambers. This geometry is shown in Fig. 24 and the geometry for all of the test fires is listed in Table 8. The thinner triple helix promotes more mixing of the center port than the double-helix design and results in more fuel between the combustion chamber and the motor wall, which allows for longer burn times. The precombustion chamber was also designed with fuel structures designed to promote flame holding and to turn the oxidizer streams, preventing their direct impingement on the opposite fuel wall. Figure 25 shows these fuel structures.

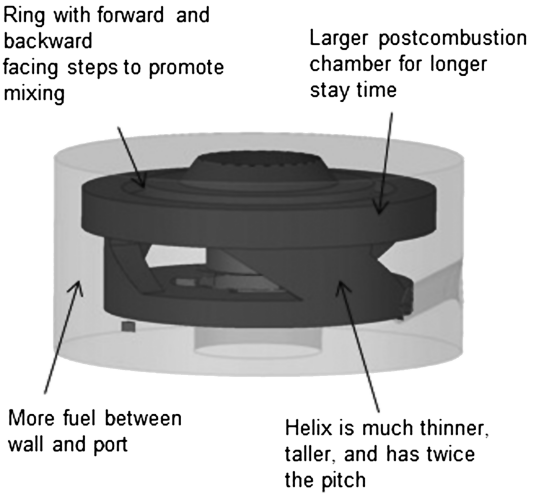

Fig. 24 Fuel grain geometry for HF6 and HF7.

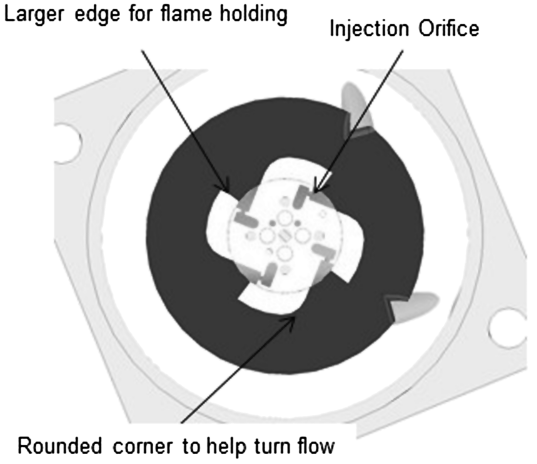

Fig. 25 Fuel grain geometry in precombustion chamber for HF6 and HF7.

As a result of this redesign, the specific impulse for HF6 and HF7 increased by approximately 16% over the previous test fires. The motor plume for these tests was also distinctly different from the previous tests. Figure 26 shows the differences in flow features between tests HF5 and HF7. Although it is difficult to capture in still photographs, the plume in HF5 shows a clear helical flame structure in addition to Mach diamonds. The plume in HF7 is much more uniform and the unmixed helical flow pattern exhibited by the previous tests is absent. It is believed by the authors that further reduction in the oxidizer mass flow rate would continue this trend, further increasing the MUPHyN specific impulse.

D. Thrust-Vectoring Test Results

Thrust-vectoring tests were completed with nitrogen, helium, and oxygen as secondary injectants. Table 9 summarizes the thrust-vectoring test results with parameters including side-force specific

Table 8 Fuel grain geometry summary

Test no.	Port area, cm^2	Helical radius, cm	Pitch, cm	Initial surface area, cm^2	No. of ports
HF1	1.59	2.74	3.81	222	2
HF2	1.54	2.73	3.81	211	2
HF4, HF5	1.59	2.74	6.35	190	2
HF6, HF7	55.2	2.91	12.7	194	3

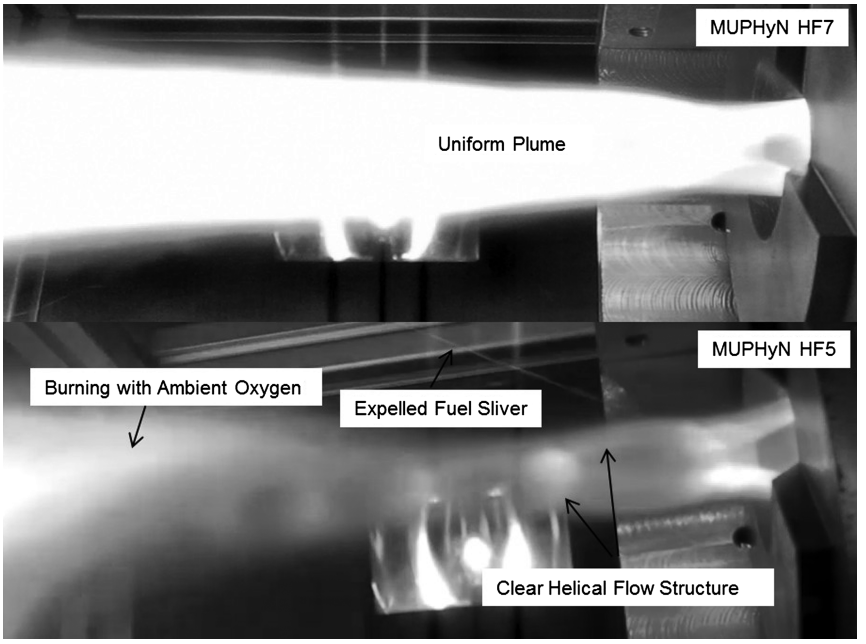

Fig. 26 Plumes for MUPHyN HF5 (double helix) and MUPHyN HF7 (triple helix).

impulse, amplification factor, and equivalent thrust vector angle for these tests with the MUPHyN motor. The side-force specific impulse is defined as

$$I_{\mathrm{sp}_s} = \frac{F_s}{\dot{m}_s g} \tag{16}$$

where F_s is the side force and $\dot{m}_s$ is the mass flow rate of the secondary injectant.

As discussed previously, secondary injection on an aerospike nozzle creates a localized bow shock in front of the injection site and increases the total generated side force. Figure 27 shows the MUPHyN plume with and without secondary injection active. When the secondary injection port is active, the shock waves created by secondary flow interaction ahead of the injection site are clearly visible.

Figures 28–30 plot the side force, specific impulse, and mass flow rates achieved using gaseous nitrogen, helium, and oxygen, respectively. The side-force impulses appear to be both crisp and repeatable. The total thrust vector angle for tests with helium was substantially higher than those with nitrogen and oxygen, due to higher injection pressures and higher total mass flow rates. The higher achieved side-force specific impulse for helium is likely a result of the significantly lower molecular weight and/or the higher specific heat ratio of the injectant. The amplification factor for oxygen was not substantially higher than that shown for nitrogen, which implies that combustion of the oxygen with unreacted fuel in the separated region before the secondary injection port does not significantly influence thrust-vectoring efficiency. The estimated uncertainty in side-force specific impulse calculations is approximately 2.0 s.

For the range of thrust-vectoring angles examined in this research effort, no discernible decrease in axial specific impulse was seen due to thrust vectoring. Because axial thrust-vectoring losses are

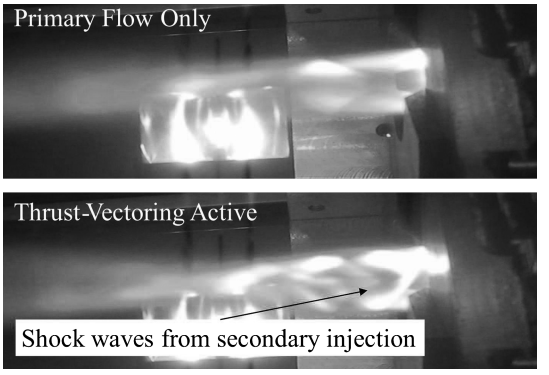

Fig. 27 MUPHyN motor plume with and without active secondary injection.

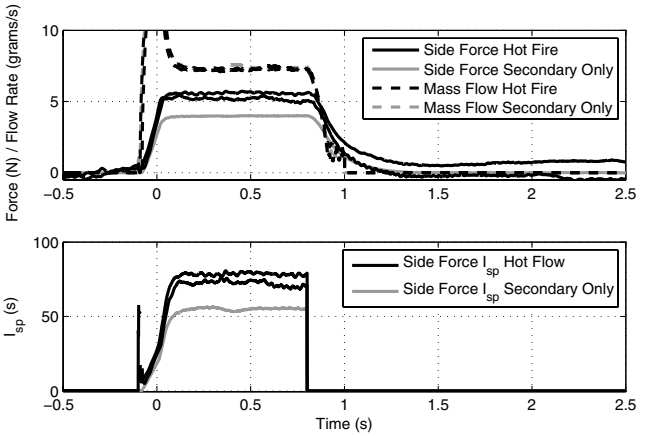

Fig. 28 Secondary flow side force, mass flow rate, and I_{sp} with nitrogen secondary injection.

Table 9 Thrust-vectoring test summary

Injectant	Secondary flow only I_{sp}, s	I_{sp} with primary flow, s	Amplification factor	Thrust vectoring angle, deg	Injectant static pressure, MPa
Nitrogen	51.0	67.1	1.32	1.95	3.5
Helium	121.3	165.5	1.36	3.63	5.7
Oxygen	55.2	73.1	1.32	2.63	3.5
Measurement uncertainty, 95%	±2.0%	±2.0%	±2.4%	±0.4%	±0.5%

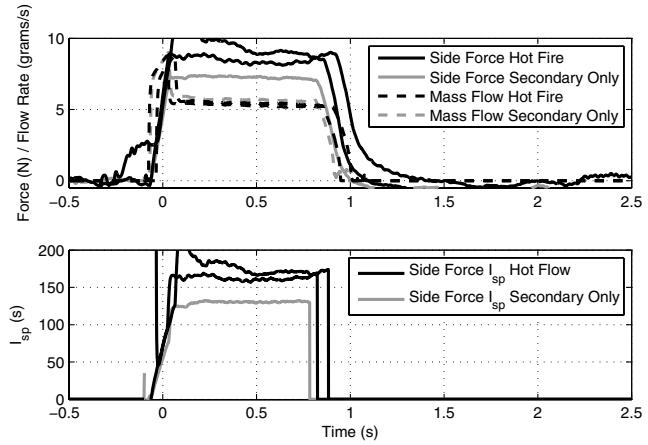

Fig. 29 Secondary flow side force, mass flow rate, and I_{sp} with helium secondary injection.

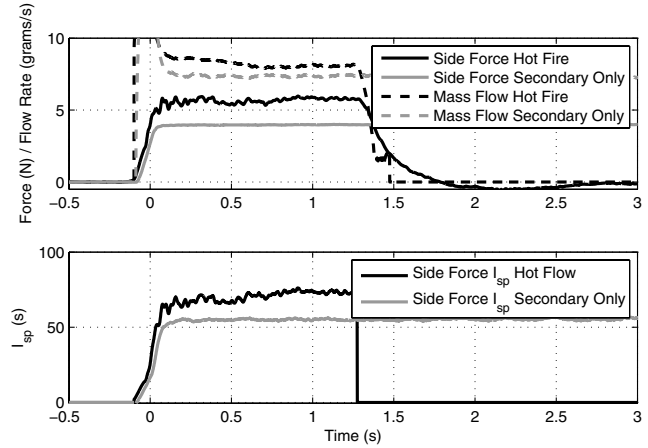

Fig. 30 Secondary flow side force, mass flow rate, and I_{sp} with oxygen secondary injection.

proportional to the cosine of the thrust-vectoring angle, this is not surprising. This effect parallels previous results from cold-flow thrust-vectoring tests on an aerospike nozzle [21].

The hot-gas side-force amplification factor (132% for nitrogen/oxygen, 136% for helium) is only slightly lower than the 139% amplification factor demonstrated by Eilers et al. [13] for cold-flow tests using CO2 gas. The collected specific impulses from both MUPHyN and CO2 gas tests are shown in Fig. 31. The uncertainties for the specific impulse measurements with CO2 gas are approximately 3.5% of the measurement and 1.1% of the measurement for tests with the MUPHyN configuration.

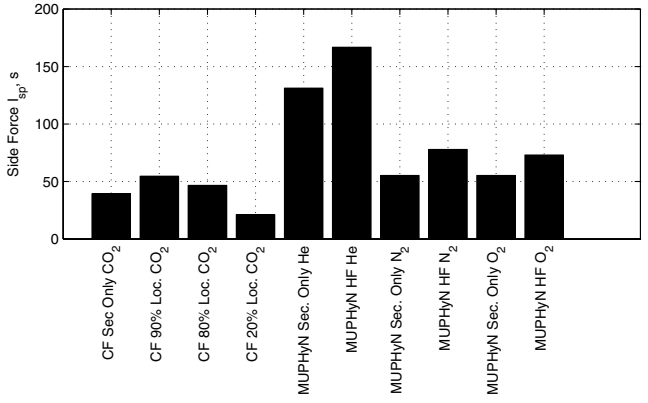

Fig. 31 Thrust-vectoring specific impulse test results for both cold-flow (CF) and MUPHyN tests, each with primary flow active and secondary-only flow configurations.

VII. Conclusions

The authors of this work have designed and tested a novel MUPHyN that is specifically targeted for cubesat- and nanosat-sized spacecraft. The MUPHyN thruster offers several features that are uniquely suited for nanosat and, particularly, cubesat applications. These features include 1) a highly compact truncated aerospike nozzle, 2) nonmechanical thrust vectoring using secondary fluid injection on the aerospike nozzle, 3) a hybrid fuel grain with an embedded helical port, and 4) a nonpyrotechnic ignition system.

The MUPHyN system provides two-axis attitude and velocity control using secondary-injection thrust vectoring without mechanical nozzle gimbals or additional reaction control thrusters. If multiple MUPHyN thrusters were incorporated on the same spacecraft, three-axis attitude control could be achieved, reducing the requirements for additional attitude control systems. Both larger impulse ΔV and small-impulse attitude control and proximity operation burns can be performed with the same system.

This synthesis of technologies is unique to the MUPHyN thruster design and no other commercial or government entity has produced comparable work that has been published in open literature. The resulting system is compact, nontoxic, nonexplosive, and uses nonpyrotechnic means for reliable motor ignition.

When fully developed, this enhanced propulsive capability could enable multiple cubesats to be deployed simultaneously by a single launch vehicle and independently repositioned, a key enabling technology for multipoint measurement science missions.

The initial series of MUPHyN motor test fires have demonstrated stable combustion and have shown thrust-vectoring effectiveness that closely reproduces previously demonstrated results achieved during cold-flow testing. The regenerative cooling system has performed effectively in all test fires to date.

The achieved main flow specific impulses were lower than expected. There are two plausible explanations for this lowered performance: 1) This initial series of tests was designed to have a higher than desirable oxidizer mass flow rate to ensure sufficient cooling, and 2) the fuel regression rate was much higher than initially anticipated. The high regression rate is presumably due to centrifugal flow effects produced by the helical port in the ABS fuel grains. These higher-than-expected regression rates resulted in O/F ratios significantly lower than the levels desired for good combustion efficiency. A MUPHyN design with lower oxidizer flow rates and a fuel grain with geometry that induced additional mixing showed significant improvement in specific impulse, and it is believed that this trend would continue for even lower flow rates.

References

[1] Isakowitz, S. J., Hopkins, J. B., Jr., and Hopkins, J. P. H., *International Reference Guide to Space Launch Systems*, AIAA, Reston, VA, 2004, pp. 53–83, 95–128.

[2] Goldstein, E., "Greening of Satellite Propulsion," *Aerospace America*, Vol. 50, 2, 2012, pp. 26–28.

[3] Safie, F. M., and Fox, E. P., "Probabilistic Design Analysis Approach for Launch Systems," *27th AIAA, SAE, ASME, and ASEE, Joint Propulsion Conference*, AIAA Paper 1991-3372, 1991.

[4] Chang, I.-S., "Investigation of Space Launch Vehicle Catastrophic Failure," AIAA Paper 1995-3128, July 1995.

[5] Maggie, G., "Space Shuttle Probabilistic Risk Assessment: Methodology and Application," *International Symposium on Product Quality and Integrity, Proceedings of the Reliability and Maintainability Symposium*, Las Vegas, NV, 1996, pp. 121–132.

[6] Schmidt, E. W., *Hydrazine and its Derivatives: Preparation, Properties, Applications*, 2nd ed., Vol. 2, Wiley-Interscience, New York, 2001, pp. 1103–1265.

[7] Sutton, G. P., and Biblarz, O., *Rocket Propulsion Elements*, 7th ed., Wiley, New York, 2001, pp. 245–269, Chap. 6.

[8] Choudhary, G., Hansen, H., Donkin, S., and Kirman, C., "Toxicological Profile for Hydrazines," *U.S. Department of Health and Human Services Public Health Service Agency for Toxic Substances and Disease Registry (ATSDR)*, Atlanta, 1997, pp. 1–224.

[9] Anon., "Hazard Analysis of Commercial Space Transportation; Vol. 1: Operations, Vol. 2: Hazards, Vol. 3: Risk Analysis," U.S. Dept. of Transportation PB93-199040, Accession No. 00620693, 1988.

[10] Chiaverini, M. J., *Fundamentals of Hybrid Rocket Combustion and Propulsion*, edited by Kuo, K. K.AIAA Publications, Reston, VA, 2007, pp. 573–632.
[11] Aerojet, "Aerojet Datasheet," http://www.aerojet.com/capabilities/2011-H-4232DataSheets.pdf [retrieved 14 April 2013].
[12] Anon., *Edison Small Satellite Flight Demonstration Missions,* NASA BAA-NNA-12ZD0001K, March 2012, http://nspires.nasaprs.com [retrieved 8 March 2012].
[13] Eilers, S. D., Wilson, M., and Whitmore, S., "Analytical and Experimental Evaluation of Aerodynamic Thrust Vectoring on an Aerospike Nozzle," *46th AIAA/ASME/SAE/ASEE Joint Propulsion Conference and Exhibit*, Nashville, TN, AIAA Paper 2010-6964, Reston, VA, 2010.
[14] Whitmore, S. A., Peterson, Z. W., and Eilers, S. D., "Analytical and Experimental Comparisons of HTPB and ABS as Hybrid Rocket Fuels," *47th AIAA/ASME/SAE/ASEE Joint Propulsion Conference & Exhibit*, San Diego, CA, AIAA Paper 2011-5909, Reston, VA, 2011.
[15] Gibbon, D., and Haag, G. S., "Investigation of an Alternative Geometry Hybrid Rocket for Small Spacecraft Orbit Transfer," Surrey Satellite Technology Technical Rept. SPBB-26287-01, 2001.
[16] Knuth, W. H., Chiaverini, M. J., Sauer, J. A., and Gramer, D. J., "Solid-Fuel Regression Rate Behavior of Vortex Hybrid Rocket Engines," *Journal of Propulsion and Power*, Vol. 18, No. 3, 2002, pp. 600–609. doi:10.2514/2.5974
[17] Whitmore, S. A., Merkley, D. P., Eilers, S. D., and Taylor, T. T., "Hydrocarbon-Seeded Ignition System for Small Spacecraft Thrusters Using Ionic Liquid Propellants," *27th AIAA/USU Conference on Small Satellites*, Utah State University, Logan, UT, AIAA Paper SSC13-VII-6, Reston, VA, 2013.
[18] Lee, C., and Thompson, D., "Fortran Program for Plug Nozzle Design," NASA TM-X-53019, 1964.
[19] Ladeinde, T., and Chen, H., "Performance Comparison of a Full-Length and a Truncated Aerospike Nozzle," *46th AIAA/ASME/SAE/ASEE Joint Propulsion Conference & Exhibit*, Nashville, TN, AIAA Paper 2010-6593, Reston, VA, 2010.
[20] Ito, T., and Fujii, K., "Numerical Analysis of the Base Bleed Effect on the Aerospike Nozzles," *Transactions of the Japan Society for Aeronautical and Space Sciences*, Vol. 46, No. 148, Aug. 2002.
[21] Eilers, S. D., Wilson, M. D., Whitmore, S. A., and Peterson, Z. W., "Side-Force Amplification on an Aerodynamically Thrust-Vectored Aerospike Nozzle," *Journal of Propulsion and Power*, Vol. 28, No. 4, 2012, pp. 811–819. doi:10.2514/1.59177
[22] Lemieux, P., "Nitrous Oxide Cooling in Hybrid Rocket Nozzles," *Progress in Aerospace Sciences*, Vol. 46, Nos. 2–3, 2010, pp. 106–115. doi:10.1016/j.paerosci.2009.12.001
[23] Lemieux, P., "Development of a Reusable Aerospike Nozzle for Hybrid Rocket Motors," *39th AIAA Fluid Dynamics Conference*, San Antonio, TX, AIAA Paper 2009-3720, Reston, VA, 2009.
[24] Lemieux, P., Murray, W. R., Mello, J. D., Cooke, T. H., and Gerhardt, J. A., "Design and Analysis of a Reusable N2O-Cooled Aerospike Nozzle for Labscale Hybrid Rocket Motor Testing," *47th AIAA/ASME/SAE/ASEE Joint Propulsion Conference & Exhibit*, San Diego, CA, AIAA Paper 2011-5909, Reston, VA, 2011.
[25] Mayer, E., "Analysis of Convective Heat Transfer in Rocket Nozzles," *ARS Journal*, Vol. 31, No. 7, 1961, pp. 911–916. doi:10.2514/8.5675
[26] Gordon, S., and McBride, B. J., "Computer Program for Calculation of Complex Chemical Equilibrium Compositions and Applications I. Analysis," NASA RP-1311, 1994.
[27] McBride, B. J., and Gordon, S., "Computer Program for Calculation of Complex Chemical Equilibrium Compositions and Applications II. Users Manual and Program Description," NASA RP-1311, 1996.
[28] Kandlikar, S. G., "A General Correlation for Saturated Two-Phase Flow Boiling Heat Transfer Inside Horizontal and Vertical Tubes," *Journal of Heat Transfer*, Vol. 112, No. 1, 1990, pp. 219–228. doi:10.1115/1.2910348
[29] Incropera, F. P., Dewitt, D. P., Bergman, T. L., and Lavine, A. S., *Fundamentals of Heat and Mass Transfer*, 6th ed., Wiley, New York, 2007, pp. 485–521, Chap. 8.
[30] Span, R., and Wagner, W., "Equations of State for Technical Applications. I. Simultaneously Optimized Functional Forms for Nonpolar and Polar Fluids," *International Journal of Thermophysics*, Vol. 24, No. 1, 2003, pp. 1–39.
[31] Span, R., and Wagner, W., "Equations of State for Technical Applications. II. Results for Nonpolar Fluids," *International Journal of Thermophysics*, Vol. 24, No. 1, 2003, pp. 41–109. doi:10.1023/A:1022362231796
[32] Span, R., and Wagner, W., "Equations of State for Technical Applications. III. Results for Polar Fluids," *International Journal of Thermophysics*, Vol. 24, No. 1, 2003, pp. 111–162. doi:10.1023/A:1022310214958
[33] Dyer, J., Doran, E., Dunn, Z., Lohner, K., Zilliac, G., and Cantwell, B., "Modeling Feed System Flow Physics for Self Pressurizing Propellants," AIAA Paper 2007-5702, 2007.
[34] Linstrom, P., and Mallard, W. (eds.), *NIST Chemistry WebBook, NIST Standard Reference Database Number 69*, National Inst. of Standards and Technology, Gaithersburg, MD, http://webbook.nist.gov [retrieved 28 June 2011].
[35] Strand, L. D., Ray, R. L., Anderson, F. A., and Cohen, N. S., "Hybrid Rocket Combustion Study," AIAA Paper 1993-2412, 1993.
[36] Eilers, S. D., and Whitmore, S., "Correlation of Hybrid Rocket Propellant Regression Measurements with Enthalpy-Balance Model Predictions," *Journal of Spacecraft and Rockets*, Vol. 45, No. 5, 2008, pp. 1010–1020. doi:10.2514/1.33804

J. Blandino
Associate Editor